

# An extended algebraic reconstruction technique (ART) for density-gradient projections: laser speckle photographic tomography

H. S. Ko, K. D. Kihm

542

**Abstract** An extended algebraic reconstruction technique (ART) is presented for tomographic image reconstruction from the density-gradient projections, such as laser speckle photography. The essence of the extended ART is that the density-gradient projection data of speckle photography (Eq. (1)) are first numerically integrated to the algebraic representation of interferometric fringe number data (Eq. (12)), which ART can readily reconstruct into the cross-sectional field. The extended ART is numerically examined by using two computer synthesized phantom fields, and experimentally by using asymmetric single and double helium jets in air. The experimentally reconstructed images were also compared with the direct measurements of helium concentration using an oxygen analyzing probe. The extended ART method shows an improved accuracy and is proposed to use to tomographically reconstruct the density-gradient projections over the previous Fourier convolution (FC) method (Liu et al. 1989).

## List of symbols

$A$	amplitude of basis function
$b$	basis function (Eq. (4))
$c$	defocusing distance (Fig. 2)
$C$	multiplicative correction vector (Eq. (8))
$d$	distance between specklegram and Young's fringe images
$f$	actual field
$\hat{f}$	guessed or intermediate objective field to be reconstructed
$H$	helium mass fraction in air
$K$	Gladstone–Dale constant ( $0.226 \times 10^{-3} \text{ m}^3/\text{kg}$ at $\lambda = 632.8 \text{ nm}$ for air at STP (Eq. (1))
$m$	magnification of parabolic mirror (Fig. 2)
$m'$	magnification of camera imaging
$M$	number of rays, or the number of meshes in the $x$ -direction
$n$	index of refraction
$N$	number of basis functions, or the number of meshes in the $y$ -direction
$P$	number of projections

$R$	oxygen mass fraction in air
$R_0$	Reference oxygen mass fraction (20.6% at STP)
$s$	coordinate on the projection plane, perpendicular to the ray direction (Fig. 1)
$s_F$	fringe spacing
$t$	coordinate parallel to the ray direction (Fig. 1)
$(x, y)$	objective field coordinate (Fig. 1)
$\alpha$	line-of-sight beam deflection angle (Eq. (1), Fig. 1 or Fig. 2)
$\delta$	amount of speckle dislocation (Fig. 2 or Eq. (9))
$\varepsilon$	line-of-sight beam deflection angle measured at the ground glass plane (Fig. 2)
$\lambda$	laser wave length [ $\lambda = 632.8 \text{ nm}$ for helium–neon laser]
$\theta$	angle of projection (Fig. 1)
$\rho$	density
$\sigma$	spread of basis function (Eq. (4))
$\Phi$	reconstruction error
$\hat{\psi}$	virtual projection of guessed objective field $\hat{f}$
$\psi_{SP}$	beam deflection angle of speckle photographic projection of actual field $f$ (Eq. (1))
$\psi_{IF}$	fringe number of interferometric projection of actual field $f$ (Eq. (10))

## 1 Introduction

Speckle photography (Françon 1979) is a nonintrusive optical technique to detect light ray refraction through an optically thin phase object of varying density field. Elaborate inversion of the measured ray refraction, thereby, will determine media density and temperature fields (Merzkirch 1987). The technique provides highly accurate measurements with spatial data resolutions smaller than 1.0 mm and its wide range of applications to various thermal and fluid engineering problems have been recently presented in a review article written by one of the authors (Kihm 1997).

Speckle photography, like most other optical measurement techniques, is a line-of-sight technique and the ray integral of the information on the refractive index gradient, normal to the ray direction, is projected as beam deflection angle into a point on the projection plane. Using the Gladstone–Dale relation,  $n = 1 + K\rho$  (Partington 1953), the projected beam deflection angle  $\alpha$  is given as a ray integral of the field density gradient (Fig. 1):

$$\psi_{SP}(s, \theta) \cong \alpha = K \int \frac{\partial \rho(x, y)}{\partial s} dt \quad (1)$$

Received: 26 June 1998/Accepted: 18 March 1999

H. S. Ko, K. D. Kihm  
Department of Mechanical Engineering, Texas A&M University,  
College Station, TX 77843-3123, USA

Correspondence to: K. D. Kihm

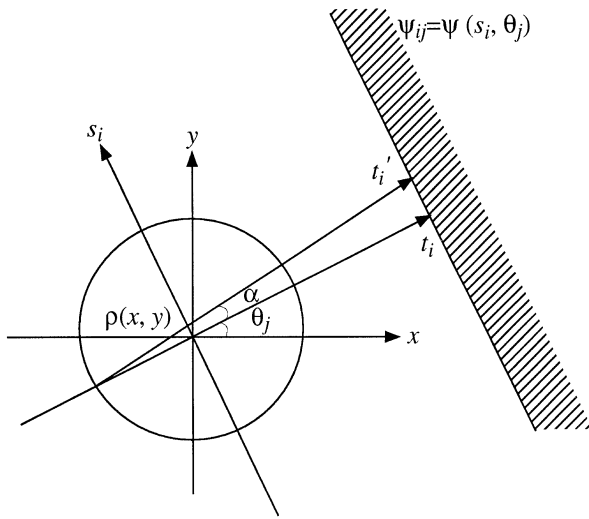


Fig. 1. Cross-sectional density field  $\rho(x, y)$  and its line-of-sight projection  $\psi_{ij} = \psi(s_i, \theta_j)$  for speckle photography

where  $s$  is perpendicular to, and  $t$  is parallel to the incident ray. The line-of-sight ambiguity in  $\alpha$ , which occurs from the ray integral along  $t$ , must be eliminated so that the true density field,  $\rho(x, y)$ , can be reconstructed. To achieve this, Eq. (1) must be somehow inverted and this mathematical inversion procedure is called tomography.

A mathematical inversion procedure for speckle photography has been developed using the two-dimensional Fourier transformation (Liu et al. 1989). This is called a Fourier convolution (FC) method, which is simple, but suffers from reduced reconstruction accuracy when the amount of projection data is limited or restricted. Due to spatial and other restrictions, the reconstruction of practical problems is viable in limited and restricted projections to a degree. An iterative reconstruction method generally works better for such cases of limited projections, because of its repeated updating of solutions. To the author's knowledge, however, no iterative reconstruction method for density-gradient projections, including speckle photography, has been published to date.

Since Eq. (1) correlating the projection and the density field is non-algebraic, the conventional algebraic reconstruction technique (ART) cannot invert Eq. (1). The present work extends ART where non-algebraic speckle photography data are numerically integrated in the projection plane to converted into algebraic interferometric data so that the latter can be converted by ART. The extended ART has been examined numerically by using computer-synthesized phantoms and experimentally using asymmetric helium jets.

## 2 Tomographic algorithms: Fourier convolutions (FC) and algebraic reconstruction technique (ART)

Fourier Convolution (FC) method is based on the Fourier slice theorem (Kak and Slaney 1987). By taking Fourier transforms on both sides of Eq. (1) and after some mathematical rearrangement, the inverse Fourier transformation is derived

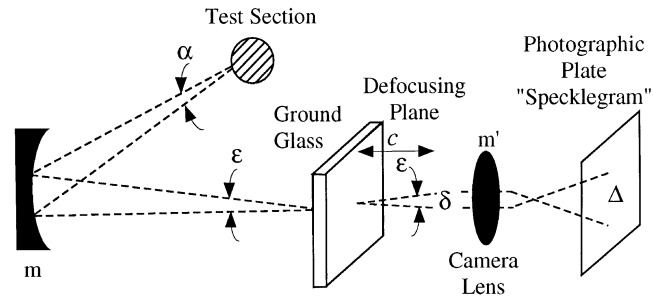


Fig. 2. Geometric formulation of speckle dislocation

to give the density distribution as (Liu et al. 1989):

$$\hat{f}(x, y) = \rho(k\Delta x, n\Delta y) = (P\pi K)^{-1} \sum_{j=0}^{N-1} \sum_{m' = -(M-1)/2}^{(M-1)/2} \alpha(m' \Delta s, j\Delta\theta) q(m - m') \quad (2)$$

where  $\hat{f}$  is an object function to be reconstructed (e.g. density field),  $\alpha$  represents the line-of-sight projected deflection angle of the refracted ray, as shown in Figs. 1 and 2,  $P$  denotes the number of projections,  $K$  is the Gladstone-Dale constant,  $k, n, j, m$ , and  $m'$  are integers, and  $\Delta x$  and  $\Delta y$  are the grid sizes in  $x$  and  $y$  directions of the  $M \times N$  discretized reconstruction plane.

The discretized filter function  $q(m)$  is given as

$$q(m) = \begin{cases} 1/m, & \text{when } m \text{ is odd} \\ 0 & \text{otherwise} \end{cases} \quad (3)$$

where  $m = \pm 1, \pm 2, \dots, \pm (M-1)/2$ . The Fourier convolution (FC) method is simple, very fast and accurate, but requires many equally angled projections for acceptable accuracy.

When using an iterative method, it is an open question concerning the best representation for the field to be reconstructed. Considering a two-dimensional cross-sectional field, one can represent the field as a series of basis functions allowing the parameters to be determined optimally:

$$\hat{f}(x, y) = \sum_{i=1}^N A_i b(x, y; \sigma_i, x_i, y_i) \quad (4)$$

where  $b$  represents a general form of basis function located at  $(x_i, y_i)$  with height  $A_i$  and spread  $\sigma_i$ , and  $N$  denotes the total number of basis functions. The use of a smooth basis function can accurately represent a relatively smooth object field with far fewer coefficients (unknowns) than a square-pixel basis function. For the field representation of Eq. (4), the number of total unknowns can be as many as  $4N$ ;  $2N$  unknown heights and spreads for the  $N$  basis functions, and  $2N$  coordinates for their locations, which can also be optimally searched (Ko et al. 1997).

The algebraic reconstruction technique (Gorden 1974) undertakes the optimization task for the linear case where each basis function is defined by a single parameter (usually its unknown height with a fixed spread) and the location of each basis function is given, i.e.,

$$\hat{f}(x, y) = \sum_{i=1}^N A_i b(x - x_i, y - y_i) \quad (5)$$

where  $A_i$  is the height coefficient of the  $i$ -th basis function centered at a specified location of  $(x_i, y_i)$ . A comparative study of the choice of basis functions (Hanson and Wecksung 1985) suggests the use of the cubic B-spline, which is described in the  $x$  variation by (Hou and Andrews 1978):

$$b_x(x-x_i) = \begin{cases} \frac{(2\Delta_x - |x-x_i|)^3 - 4(\Delta_x - |x-x_i|)^3}{4\Delta_x^3}, & |x-x_i| < \Delta_x \\ \frac{(2\Delta_x - |x-x_i|)^3}{4\Delta_x^3}, & \Delta_x \leq |x-x_i| \leq 2\Delta_x \\ 0, & |x-x_i| > 2\Delta_x \end{cases} \quad (6)$$

where  $b_x$  is equal to 1 at  $x=x_i$ , 0.25 at  $x=x_i \pm \Delta_x$ , 0 at  $x=x_i \pm 2\Delta_x$  and thereafter. The  $y$  variation  $b_y$  is similar, and the two-dimensional basis function is the product of the two, i.e.,  $b(x-x_i, y-y_i) = b_x(x-x_i) \times b_y(y-y_i)$ . All reported ART results in this paper use the cubic B-spline basis function.

The basic ART uses feedback information on the deviation of the virtual projection from the measured projection and iteratively optimizes the object coefficient vector  $A_i$  by a simple algebraic updating:

$$A_i^{q+1} = A_i^q + W_i^q \frac{\sum_p (\psi_p - \hat{\psi}_p)}{NP} \quad (7)$$

where  $W_i$  is the weighting factor and  $q$  denotes the  $q$ th iteration. An optimized set of unknown  $A_i$ 's must be found to minimize the deviations between the virtual projection  $\hat{\psi}$  of an intermediate object function  $\hat{f}$  and the measured projection  $\psi$  of the actual field  $f$ .

Multiplicative algebraic reconstruction technique (MART) differs from the ART only in the way the deviation between the virtual projection  $\hat{\psi}$  and the measured projection  $\psi$  is distributed among the object coefficients. The MART uses an element  $C_i$  of the multiplicative correction vector  $C$  as follows:

$$A_i^{q+1} = C_i^q A_i^q$$

$$C_i^q = \begin{cases} 1 - 0.5W_i^q \left(1 - \frac{\psi_i}{\hat{\psi}_i}\right), & \hat{\psi}_i \neq 0 \\ 1 & \text{otherwise} \end{cases} \quad (8)$$

where  $q$  denotes the  $q$ th iteration and  $W_i$  is the weighting factor. One advantage of using MART is to ensure a non-negative object field in reconstructing non-negative scalars.

Note that the ART and the MART updates, in principle, are possible only for algebraic projections in which the ray integration of the field directly gives the projection data, such as in interferometry (Eq. (10) in the next section).

### 3 Line-of-sight projections: laser speckle photography and interferometry

The refractive index variation of a phase object deflects the incident laser beam. The beam deflection angles or its interfered pattern with undeflected beams are projected in a line-of-sight manner on the recording plane. Laser speckle photography records the projected beam deflection angles on a double-exposed photographic film. Wave-front inter-

ferometry, such as Mach-Zehnder interferometry (Vest 1979), records the interfered fringe patterns.

The beam deflection angle of speckle photography (Fig. 2) is given as a ray integral of the field density gradient normal to the incident ray, as expressed in Eq. (1). When coherent light is incident upon the random diffraction grating, usually made of ground glass, the light rays randomly diffract in all directions in a constructive or destructive way. When viewed from a distance, the constructive or destructive interference will be seen as very fine patterns of bright and dark spots, or *laser speckles*. The change in the index of refraction of the test field will bend the ray slightly from its original path. This causes the incident ray to strike the ground glass at a slightly different angle and the speckle dislocates by an amount  $\delta$ , from its original location.

A specklegram is taken by photographically overlapping the original speckles without a test field, and then the dislocated speckles in the presence of a test field. Thus, the dislocation  $\delta$  represents the beam deflection through  $\varepsilon$ , i.e.,

$$\delta = c \tan \varepsilon = c \tan(\alpha/m) \cong c\alpha/m \quad (9)$$

where the defocusing distance  $c$  is the distance between the ground glass and the actual image plane for specklegram recording, and  $m$  is the magnification of the parabolic mirror. The amount of speckle dislocation calculates the beam deflection angle and the local value of the refractive index gradient. The measured distribution of the refractive index gradient determines the medium temperature and its gradient for diverse thermal flow problems (Wernekinck et al. 1985; Kastell et al. 1992; Kihm et al. 1993).

Wave front interferometry, such as Mach-Zehnder interferometry, creates the path length difference between the reference beam and the test beam that goes through a phase object. The resulting fringes are then shifted with respect to the undisturbed fringes (fringes formed by the two beams without a tested phase object) and the fringe shift number is expressed as

$$\psi_{IF} = \frac{1}{\lambda} \int (n - n_{\text{ref}}) dt = \frac{K}{\lambda} \int_{-\infty}^{\infty} (\rho - \rho_{\text{ref}}) dt \quad (10)$$

where  $\lambda$  denotes the laser wave length. Note that the fringe shift number is determined directly by the ray integration of the density field, whereas the beam deflection angle of laser speckle photography is given by the ray integration of the density gradient, shown in Eq. (1).

Combining Eqs. (1) and (10) gives

$$\frac{\partial \psi_{IF}}{\partial s} = \frac{K}{\lambda} \frac{\partial}{\partial s} \int (\rho - \rho_{\text{ref}}) dt = \frac{K}{\lambda} \int \frac{\partial \rho}{\partial s} dt = \frac{1}{\lambda} \psi_{SP} \quad (11)$$

Integrating Eq. (11) along  $s$  on the projection plane gives

$$\psi_{IF} = \frac{1}{\lambda} \int \psi_{SP} ds \quad (12)$$

Equation (12) states that an integral of the ray deflection angle from speckle photography,  $\psi_{SP}$ , along  $s$  is equivalent to the interferometric fringe shift number  $\psi_{IF}$ . Once the integration is carried out, the ART operator, Eqs. (7) and (8), can proceed in updating by using the straightforward feedback information on the density itself.

The idea of the density-gradient integration has been explored previously for different optical technique in using the Hartmann sensor to measure the flow field of a phase object (McMackin et al. 1995). The Hartmann sensor uses a lenslet array to split a single laser beam into a number of subapertures and detects their individual focal spot intensity patterns change occurring by the optical path differentials of the phase object. However, their application is limited to an axisymmetric tomographic reconstruction using the Abel transformation principle, which is a subset of the Fourier convolution for axisymmetric flows.

#### 4

##### Phantom reference fields and reconstruction errors

The extended ART is tested using two different computer synthesized phantom density fields that have been suggested as reference fields in previous literature (Verhoeven 1993). The first one is called a Cosine phantom expressed by:

$$f(x, y) = \begin{cases} \frac{\rho(x, y) = \frac{1 - \cos\{2\pi(x+0.5)^{4/5}\} - 1 - \cos\{2\pi(y+0.5)^{2/3}\}}{4}}{4}, & |x, y| < 0.5 \\ 0 & \text{otherwise} \end{cases} \quad (13)$$

which constructs an asymmetric single peak shown in Fig. 3a. The second phantom is called a CosGauss function by

$$f(x, y) = 0.327 \text{Cosine}(x, y) + 0.872 \exp\{-[9(x-0.2)]^2 - [6(y-0.1)]^2\} + 0.872 \exp\{-[8(x+0.2)]^2 - [30(y+0.35)]^2\} \quad (14)$$

which gives an asymmetric double-peak phantom shown in Fig. 3b.

Four different error measures are used in this paper. The first is the average error of the reconstructed object function  $\hat{f}$  and the reference phantom function  $f$ :

$$\Phi_{\text{avg}} = \frac{\sum_{i=1}^N |f(x_i, y_i) - \hat{f}(x_i, y_i)|}{N} \quad (15)$$

where  $N$  is the total number of the basis functions used to conform to the reconstructing object functions. The second is a normalized RMS error:

$$\Phi_{\text{rms}} = \sqrt{\frac{\sum_{i=1}^N [f(x_i, y_i) - \hat{f}(x_i, y_i)]^2}{\sum_{i=1}^N [f(x_i, y_i) - \bar{f}]^2}} \quad (16)$$

where  $\bar{f}$  is the average value of the phantom field  $f$ . The third one is a normalized absolute error:

$$\Phi_{\text{abc}} = \frac{\sum_{i=1}^N |f(x_i, y_i) - \hat{f}(x_i, y_i)|}{\sum_{i=1}^N |f(x_i, y_i)|} \quad (17)$$

Note that these three errors measure the reconstruction quality based on the comparison between the reconstructed field (object function) and the true field (phantom function). In real experiments, however, the true field is unknown and the quality of reconstruction is only measured by comparing the virtual projections  $\hat{\psi}$  against the measured projections  $\psi$ . Thus,

the fourth and the practically available measure of projection error is defined as

$$\Phi_{\text{pro}} = \frac{\sum_{i=1}^M \sum_{j=1}^P |\psi(s_i, \theta_j) - \hat{\psi}(s_i, \theta_j)|}{\sum_{i=1}^M \sum_{j=1}^P |\psi(s_i, \theta_j)|} \quad (18)$$

where  $M$  is the number of rays per projection and  $P$  denotes the number of projections.

#### 5

##### Reconstruction of test phantoms

The three reconstruction algorithms, ART, MART, and FC, were used for reconstruction of the two phantom fields under the speckle projections. For the Cosine phantom each projection consists of 45 rays ( $M=45$ ); the object field is described by  $15 \times 15$  discrete pixels for the FC reconstruction ( $N=225$ ), and by  $15 \times 15$  cubic B-spline basis functions for the ART and MART ( $N=225$ ). For the case of CosGauss phantom each projection consists of 63 rays ( $M=63$ ) and the number of

pixels or basis functions is  $N=25 \times 25=625$  for FC, ART and MART. When the ART iteration exceeds the optimum iteration steps, artifacts may violate the convergence resulting in gradually increasing errors (Decker 1993). Thus, the ART calculations are ceased when the minimum is reached for the discrepancy between the reconstructed field and the phantom field.

The reconstruction calculations were performed with five equally angled projections ( $P=5$ ). Figure 4 shows example projection data that are projected in the direction normal to the broadside of the Cosine phantom field. The dashed curve shows laser speckle photographic projection  $\psi_{SP}$  (Eq. (1)), and the solid curve represents its integral along the  $s$ -coordinate on the projection plane (Eq. (12)), i.e., interferometric projection  $\psi_{IF}$ . After the discrete speckle data are curve-fitted by a high-order polynomial function, the numerical integration is carried out with very fine mesh resolution. A trapezoidal rule was used for the numerical integration and no significant numerical integration error is shown to contribute to the overall reconstruction error.

The FC reconstructs the Cosine phantom within an acceptable accuracy (Fig. 3c), primarily because of the simplicity of the slightly off-centered single peak. However, the reconstruction of the double-peak phantom of the CosGauss function (Fig. 3d) shows noisy and erroneous data. In addition to the noise arising near the field boundary, four or more misrepresenting peaks are present.

The extended ART reconstructs the Cosine phantom in a better accuracy (Fig. 3e). The ART reconstruction of the CosGauss phantom (Fig. 3f) shows significant improvement over the FC reconstruction of Fig. 3d. The two peaks are clearly pronounced and the peak locations are accurately predicted. The peak heights, however, are 15–20% underpredicted compared with the phantom heights. It is believed that this

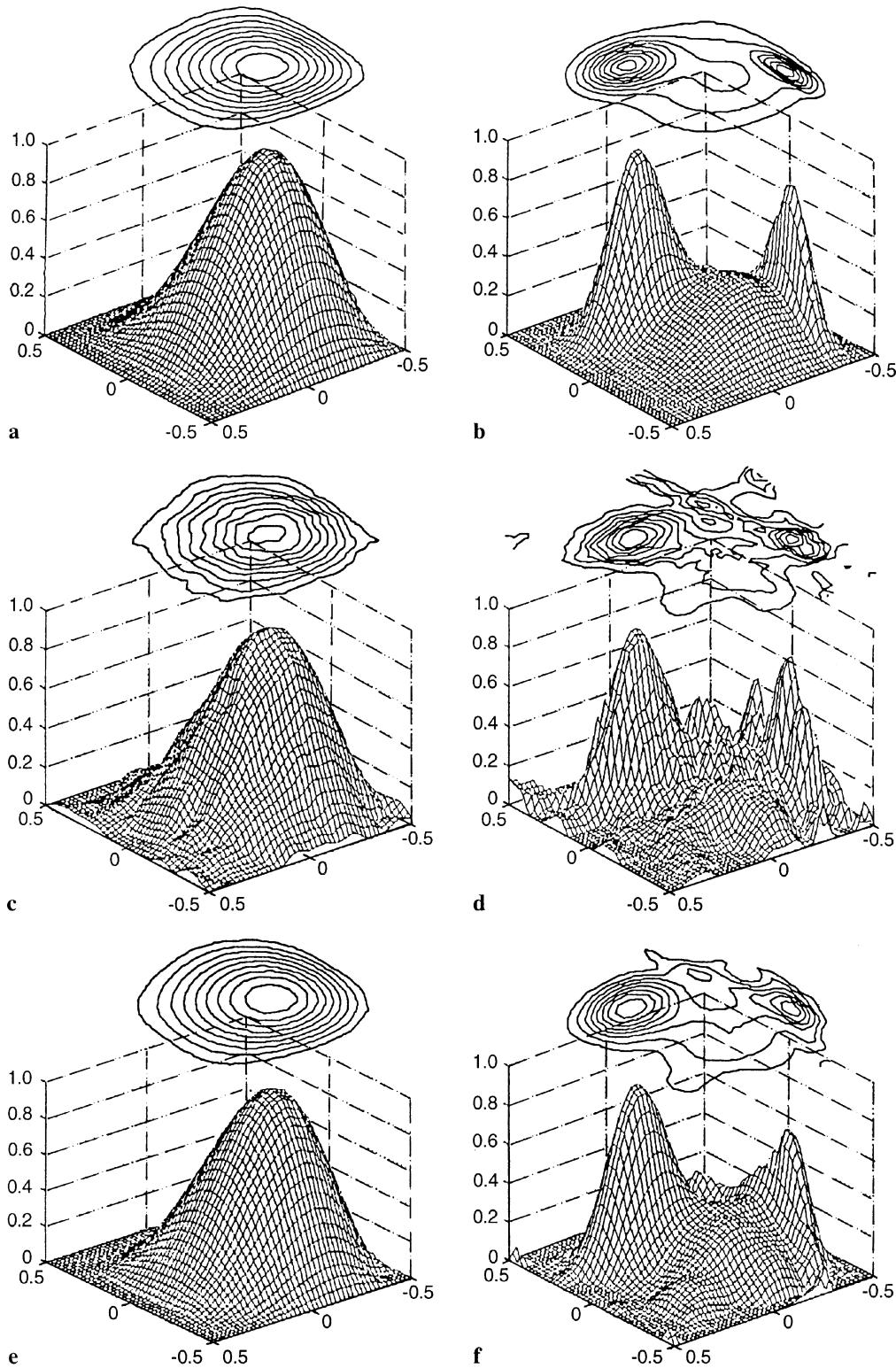


**Fig. 3a–f.** Reference phantom fields and their reconstructions for speckle photography under five projections. **a** Cosine phantom; **b** CosGauss phantom; **c**, **d** FC reconstructions; **e**, **f** ART reconstructions

discrepancy can be attributed primarily to the numerical diffusion due to the discrete representation of the phantom field using the basis function. Nevertheless, the extended ART method shows a noticeably improved reconstruction performance in comparison with the FC method.

Table 1 presents a comparison of the four errors (Eqs. (15)–(18)) for the reconstruction results shown in Fig. 3. The average, RMS, and absolute errors are various measures of the reconstruction accuracy for the reference phantom field. These errors have more significance when comparing

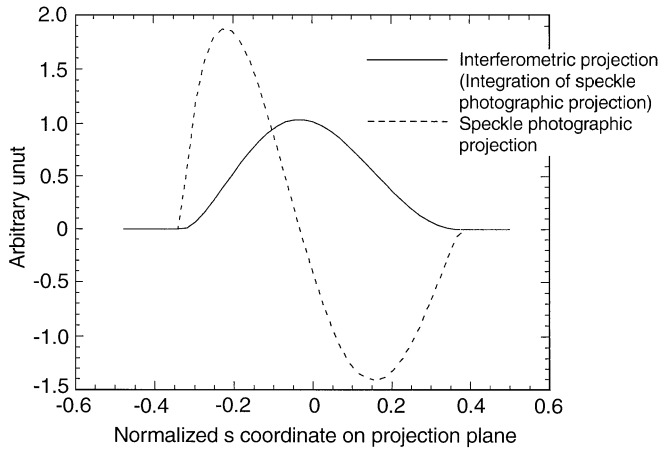


Fig. 4. Integration of speckle photographic projection and conversion to interferometric projection of Cosine function

Table 1. Comparison of reconstruction errors between the extended algebraic reconstruction technique (ART), multiplicative ART (MART), and Fourier convolution (FC) method

Number of projections	Phantom field	Reconstruction technique	$\Phi_{avg}$	$\Phi_{rms}$	$\Phi_{abs}$	$\Phi_{pro}$
3	Cosine	ART	2.98	14.70	12.73	12.06
		MART	2.28	12.64	9.72	10.38
		FC	8.98	40.58	38.33	—
	CosGauss	ART	4.65	38.58	33.59	17.65
		MART	4.03	38.43	29.08	14.32
		FC	10.84	93.41	78.30	—
5	Cosine	ART	0.93	5.07	3.99	5.79
		MART	1.07	6.01	4.58	3.34
		FC	2.85	12.97	12.15	—
	CosGauss	ART	2.50	22.75	18.06	5.94
		MART	2.45	25.76	17.69	6.61
		FC	5.16	43.34	37.26	—

tomographic algorithms using a *known* reference field. For all the tested cases, the reconstruction errors of ART are significantly lower than those of the FC method.

In reality, since the reference field is unknown and yet to be determined, the projection error (Eq. (18)) is the only available measure of the reconstruction accuracy. The projection errors of the FC results would not truly reflect the deviations of the reconstructed field from the reference phantom field since the projection errors will be dominated by the numerical errors occurring from the differentiation of the discretely reconstructed field, which is necessary for  $\hat{\psi}$  in Eq. (18).

While the errors of the MART results are slightly, but consistently, smaller than those of the ART for three projection cases, the errors of the ART and the MART are comparable for five projection cases, showing poor performances of the MART than the ART for some cases. Verhoeven (1993) recommends MART, instead of ART, particularly for non-negative scalar fields like a density field. However, since the errors between the ART and the MART are not much different and some cases are

reversed, the presented results herein will focus only on the ART.

## 6 Experimental setup

Two asymmetric helium jets, one from a half-blocked orifice (Fig. 5a) and the other from a two-hole orifice (Fig. 5b), were tested for the extended ART reconstruction from the speckle photographic projections. Both orifices were installed at the end of 12.7 mm ID copper tube. For detailed positioning, the entire jet unit sits on a rotational, and vertically adjustable stand. Line-of-sight speckle photographic images were taken at four equally-angled projections with 45 data realizations per projection for the half-blocked jet, and at six equally-angled projections with 85 projection data points for the two-hole jet. A Pitot tube measured flow velocity profiles at the tube exit, which converted to the spatially averaged velocity and Reynolds number.

The present speckle photography system uses a 35 mW He-Ne laser ( $\lambda=632.8$  nm) as the light source. A  $4 \times 5$  format camera ( $f=5.6$  at  $1/250$  s) records superimposed speckle images, with and without a test field. The photographic negative of speckle images is mounted to a precise  $x$ - $y$  stage and is interrogated by a 10 mW He-Ne laser with a beam diameter of 0.8 mm. At each illuminated point on the speckle-gram, Young's fringes are generated and the fringe images are recorded by a CCD camera and digitized into a PC to measure the fringe spacing,  $s_F$  (Robinson 1983). The beam deflection angle is given as (Kastell et al. 1992):

$$\alpha = \frac{m \lambda d}{m' c s_F} \quad (19)$$

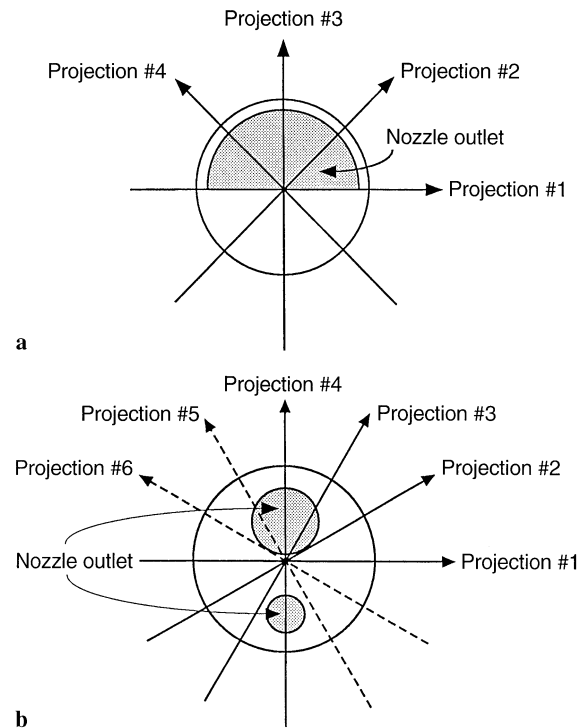


Fig. 5a, b. Schematic of a half-blocked nozzle and b two-hole nozzle

where  $c$  is the defocusing distance (Fig. 2),  $d$  is the distance between the specklegram and the imaging screen for Young's fringes, and  $m$  and  $m'$  denote the magnification of the parabolic mirror and the camera, respectively. The beam deflection

angle, Eq. (19), constitutes the line-of-sight speckle photographic projections of Eq. (1).

The oxygen analyzer directly measures the density of air/helium mixture by detecting the oxygen percentage of sampled gas (Fumizawa and Okamoto 1993). The principle of the analyzer is based on a Zirconia sensor that measures the quantity of oxygen ions at an elevated temperature. The oxygen percentage can be easily converted to the gas density  $\rho$  as follows:

$$\rho = H * \rho_{\text{he}} + (1 - H) * \rho_{\text{air}} \quad \text{with} \quad H = 1 - R/R_0 \quad (20)$$

where  $H$  is the helium mass fraction,  $R$  is the measured oxygen percentage,  $R_0$  is the reference oxygen percentage (20.6% at the laboratory),  $\rho_{\text{he}}$  is the pure helium density, and  $\rho_{\text{air}}$  is the pure air density given at the laboratory. The measured gas density is readily converted to normalized helium concentration as

$$\rho^* = \frac{\rho - \rho_{\text{air}}}{\rho_{\text{he}} - \rho_{\text{air}}} \quad (21)$$

where  $\rho^*$  ranges from 0 for pure air to 1.0 for pure helium. This normalized helium concentration is used as the reference profiles for the comparison of the optically measured density profiles.

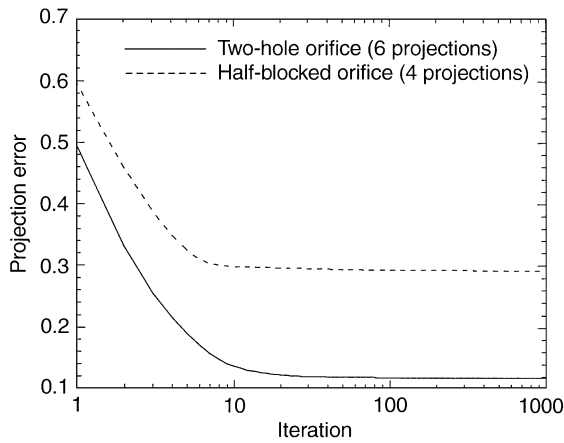


Fig. 6. Projection errors versus iteration for ART reconstruction of experimental data

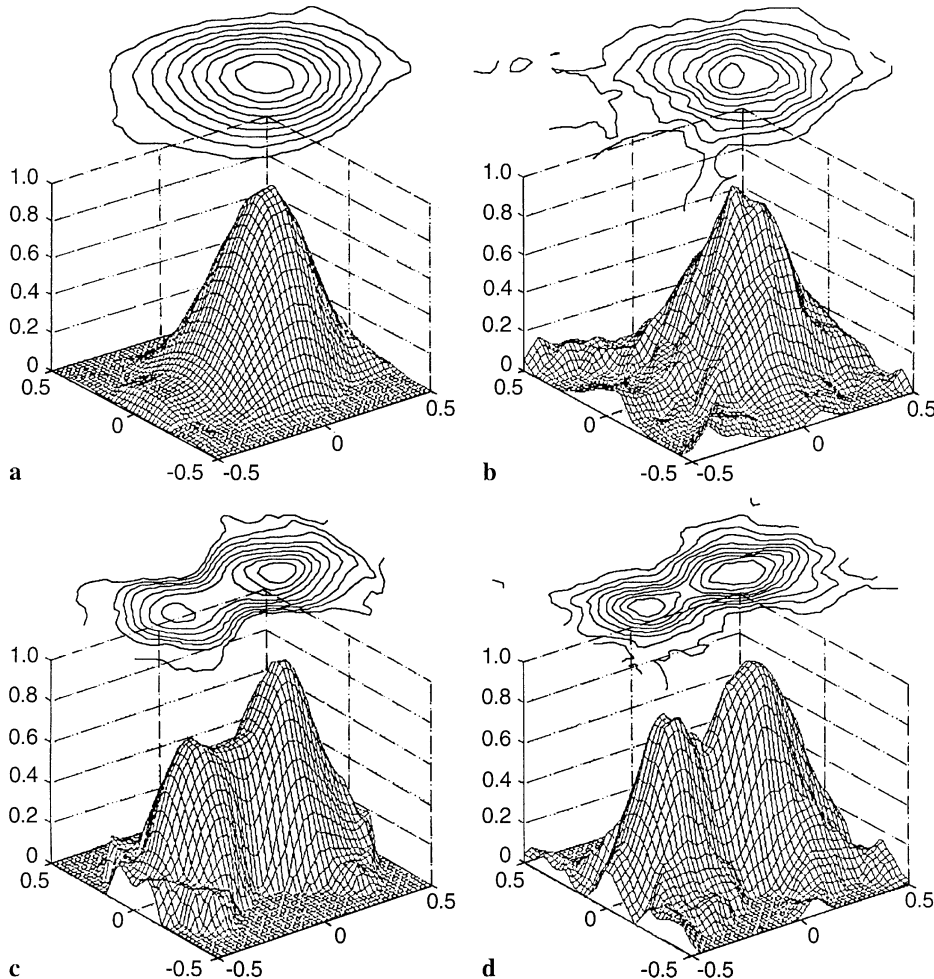


Fig. 7a-d. Reconstructed fields using extended ART and FC: half-blocked orifice ( $Re = 990$ ) a ART; b FC; two-hole orifice ( $Re = 1270$ ); c ART d FC

## Experimental results

15 × 15 cubic B-spline basis functions were used to constitute the cross-sectional object field of the half-blocked jet and 25 × 25 cubic B-spline functions were used to constitute the two-hole jet. The regression technique fitted the discrete projection data (45 or 85 data points per projection) to the ninth-order polynomials and the polynomials were analytically integrated to the interferometric data for the successive ART reconstruction. An initial guess of zero helium concentration in the whole domain was used for both calculations.

Figure 6 shows the projection errors (Eq. (18)) versus the ART iteration steps for the two tested cases. Since the true density field is unknown, the reconstruction errors based on the real field ( $\Phi_{\text{avg}}$ ,  $\Phi_{\text{rms}}$ ,  $\Phi_{\text{abs}}$ ) cannot be evaluated and the only available error for the real application of ART is the projection error  $\Phi_{\text{pro}}$ . The two-hole jet reconstruction updates the guessed field six times per iteration using its six projection data sets, whereas the half-blocked jet reconstruction updates only four times per iteration from its four projection data sets. This 50% more number of updates for the two-hole jet results in lower values of projection errors compared with the half-blocked jet. On the other hand, the projection errors of the half-blocked jet reach the minimum value more quickly than the two-hole jet, which is attributed to the simpler nature of the single-peaked, half-blocked jet.

Figures 7a and c show the ART reconstruction results of normalized helium concentration, and Figs. 7b and d show the FC reconstruction results under four projections for the half-blocked nozzle and six projections for the two-hole orifice. The reconstruction for all the present cases was carried out for the cross-section located 9.0 mm above the orifice. The helium jet was maintained laminar at  $Re = 990$  for the half-blocked orifice, based on the tube inner diameter  $D = 12.7$  mm, and  $Re = 1270$  for the two-hole orifice.

The ART reconstruction results in Fig. 7 show smoother density fields and lower noise than the FC results. The ART results contain virtually no directional dependence and no ambiguities outside the jet regions. The use of cubic B-spline basis functions helps to reconstruct smoother and more comprehensive fields. The FC results, however, show noisy and immature reconstruction compared with the ART results. The square-pixel construction of the objective field in FC produces the discretized results showing bumps in the field. The FC results also show a strong directional dependence with enlarged noise along the projection directions. Non-zero values outside the jet are believed to be the mathematical artifacts due to the only 4 (half-blocked jet) or 6 (two-hole jet) projections that are insufficient for the one-time analytical inversion of FC calculation.

Figure 8 shows the reconstructed results along the symmetric lines, as oriented vertically in Fig. 5, in comparison with the measured helium concentration using the oxygen sensor probe. The solid circles represent the average oxygen sensor readings and the fluctuating ranges are marked with the uncertainty bars for the peak reading cases. The extended ART results (solid curves) show more accurate identification of the peaks and agree more quantitatively with the oxygen probe results. The FC results (dashed curves) do not accurately predict the peak locations and slopes. The deviations of the FC

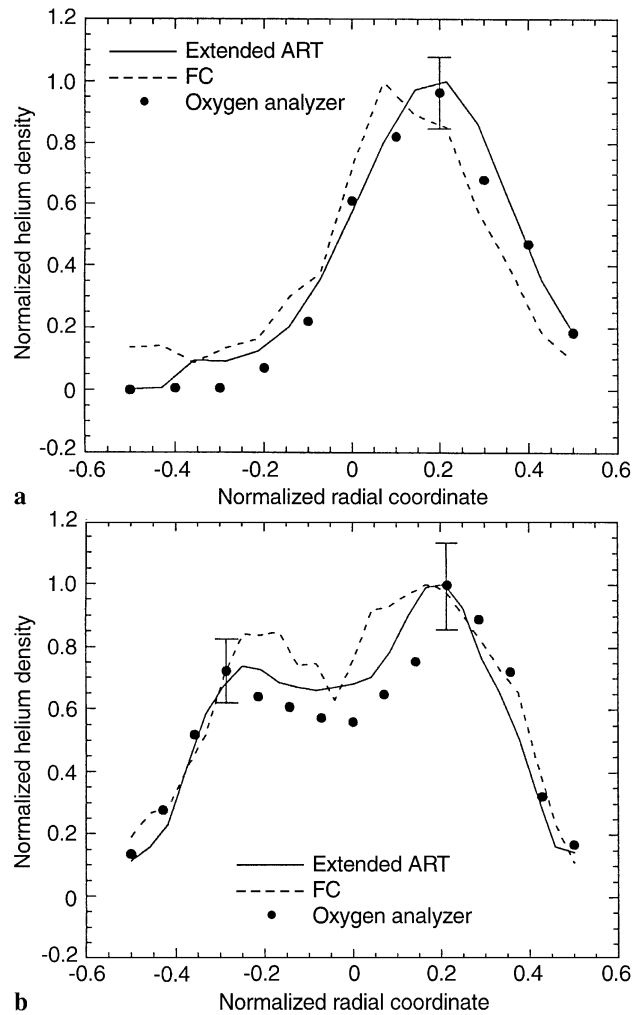


Fig. 8a, b. Comparison of normalized helium density distribution along the centerline of a half-blocked orifice ( $Re = 990$ ), and b two-hole orifice ( $Re = 1270$ ) for extended ART reconstructions, FC reconstructions, and oxygen analyzer data

results from the direct measured data, and the ART data, are more pronounced for the twin peak distributions of the two-hole jet.

## 8 Concluding remarks

The extended algebraic reconstruction technique (ART) is developed for the purpose of using tomographic reconstruction of density-gradient optical projection method. The present study focuses on speckle photography diagnostics, but the new extended ART method can be applied to additional density-gradient projection diagnostics, such as schlieren and shearing interferometry. The extended ART converts nonalgebraic speckle projection data into algebraic interferometric projections so that the conventional ART iteration process can proceed. The accuracy and efficacy of the new ART scheme were examined computationally by using computer synthesized phantom fields and experimentally by the use of asymmetric helium jets. In comparison with the Fourier convolution (FC) reconstruction, ART shows significant

improvement in reconstruction accuracy and smoothness. Also, the ART results show good agreement with the direct measurement of helium concentration distributions using an oxygen analyzing sensor.

## References

- Decker TJ (1993) Tomographic methods in flow diagnostics. NASA Report No. 106330
- Françon M (1979) Laser speckle and applications in optics. New York: Academic Press.
- Fumizawa M; Okamoto K (1993) Mole fraction distribution in a slow jet forming a stably stratified field. *Kerntechnik* 58: 32–36
- Gordon R (1974) Tutorial on algebraic reconstruction technique. *IEEE Trans NS-21*: 78–92
- Hanson KM; Wecksung GW (1985) Local basis function approach to computed tomography. *Appl Opt* 24: 4028–4039
- Hou HS; Andrews HC (1978) Cubic splines for image interpolation and digital filtering. *IEEE Trans Acoust. Speech Signal Process* 26: 508–517
- Kak AC; Slaney M (1987) Principles of computerized tomographic imaging. New York: IEEE Press
- Kastell D; Kihm KD; Fletcher LS (1992) Study of laminar thermal boundary layers occurring around the leading edge of a vertical isothermal wall using a specklegram technique. *Exp Fluids* 13: 249–256
- Kihm KD (1997) Laser speckle photography technique applied for heat and mass transfer problems. *Adv Heat Transfer* 30: 255–311
- Kihm KD; Kim JH; Fletcher LS (1993) Investigation of natural convection heat transfer in converging channel flows using a specklegram technique. *J Heat Transfer* 115: 140–148
- Ko HS; Lyons DP; Kihm KD (1997) A comparative study of algebraic reconstruction technique (ART) and genetic algorithm (GA) for beam deflection tomography. ASME Fluid Engineering Division Summer Meeting, Paper No. FEDSM97-3104, Vancouver, Canada
- Liu TC; Merzkirch M; Oberste-Lehn K (1989) Optical tomography applied to speckle photographic measurement of asymmetric flows with variable density. *Exp Fluids* 7: 157–163
- Merzkirch W (1987) Flow visualization. 2nd ed. New York: Academic Press
- McMackin L; Masson B; Clark N; Bishop K; Pierson R; Chen E (1995) Hartmann wave front sensor studies of dynamic organized structure in flowfields. *AIAA Journal* 33: 2158–2164
- Partington JR (1953) An advanced treatise on physical chemistry. Physico-chemical optics IV. Green, London: Longmans
- Robinson DW (1983) Automatic fringe analysis with a computer image-processing system. *Appl Opt* 22: 2169–2176
- Verhoeven D (1993) Limited-data computed tomography algorithms for the physical sciences. *Appl Opt* 32: 3736–3754
- Vest, CM (1979) Holographic interferometry. New York: Wiley
- Wernekinck U; Merzkirch W; Fomin NA (1985) Measurement of light deflection in a turbulence density field. *Exp Fluids* 3: 206–208